

# Spatial and temporal coherence between Amazon River discharge, salinity, and light absorption by colored organic carbon in western tropical Atlantic surface waters

J. Salisbury,<sup>1</sup> D. Vandemark,<sup>1</sup> J. Campbell,<sup>1</sup> C. Hunt,<sup>1</sup> D. Wisser,<sup>2</sup> N. Reul,<sup>3</sup> and B. Chapron<sup>3</sup>

Received 26 January 2011; revised 7 April 2011; accepted 20 April 2011; published 23 July 2011.

[1] The temporal evolution and spatial distribution of surface salinity and colored detrital matter (cdm) were evaluated within and adjacent to the Amazon River Plume. Study objectives were as follows: first, to document the spatial coherence between Amazon discharge, salinity, cdm, and the nature of the salinity-cdm relationship; second, to document the temporal and spatial variability of cdm along the trajectory of the low-salinity Amazon Plume, and third, to explore the departure of cdm from conservative mixing behavior along the plume trajectory into the open ocean. Time series (2003–2007) of surface salinity estimated using the Advanced Microwave Scanning Radiometer–Earth Observing System and corresponding satellite cdm absorption (acdm) data documented a plume of freshened, colored water emanating from the Amazon. Salinity and acdm were generally coherent, but there were regions in which spatial patterns of salinity and acdm did not coincide. Salinity was oppositely phased with discharge, whereas acdm was in phase but lagged discharge and typically remained high after maximum discharge. Along the river plume trajectory, acdm was inversely correlated with salinity, yet there was considerable deviation from conservative mixing behavior during all seasons. Positive anomalies in a linear relationship between salinity and acdm corresponded to areas of enhanced satellite-retrieved net primary productivity, suggesting the importance of phytoplankton biomass or its subsequent remineralization as a source of cdm. Negative anomalies tended to predominate at the distal sections of the plume trajectories, an observation consistent with the process of photo-oxidation of cdm over observed time scales of days to weeks.

**Citation:** Salisbury, J., D. Vandemark, J. Campbell, C. Hunt, D. Wisser, N. Reul, and B. Chapron (2011), Spatial and temporal coherence between Amazon River discharge, salinity, and light absorption by colored organic carbon in western tropical Atlantic surface waters, *J. Geophys. Res.*, 116, C00H02, doi:10.1029/2011JC006989.

## 1. Introduction

[2] The plumes of major rivers are sites of intense biogeochemical transformation [McKee *et al.*, 2004] and ecological complexity [Hickey *et al.*, 2010]. While global ocean satellite data presently provide a unique ability to resolve spatial and temporal variability in sea surface temperature and various biogeochemical indices, key gaps in our knowledge of plume biogeochemistry could be addressed if accurate satellite salinity data were also available.

[3] The Amazon River, whose average discharge at Obidos, Brazil, is  $(1.55 \times 10^5 \pm 0.13) \text{ m}^3 \text{ s}^{-1}$  is by far the largest single source of terrestrial freshwater to the ocean and contributes about 30% of total river discharge to the Atlantic Ocean [Wisser *et al.*, 2010]. Its flow is distinctly seasonal with minimum discharge occurring in November ( $\sim 0.8 \times 10^5 \text{ m}^3 \text{ s}^{-1}$ ) and maximum discharge occurring in late May ( $2.4 \times 10^5 \text{ m}^3 \text{ s}^{-1}$ ) [Lentz, 1995]. This flux impacts surface ocean density in the Caribbean more than 3500 km from the Amazon source [Hellweger and Gordon, 2002], and causes a surface discoloration readily detectable in satellite ocean color data that can extend over areas as large as 500,000 km<sup>2</sup> [Muller-Karger *et al.*, 1988, 1995; Longhurst, 1995; Hu *et al.*, 2004; Fratantoni and Glickson, 2002; Del Vecchio and Subramaniam, 2004].

[4] Amazon water enters the Western Tropical Atlantic near the equator (Figure 1) and is carried northwestward along the Brazilian Shelf by the North Brazilian Current (NBC) [Muller-Karger *et al.*, 1988, 1995]. Although some

<sup>1</sup>Ocean Processes Analysis Laboratory, University of New Hampshire, Durham, New Hampshire, USA.

<sup>2</sup>Water Systems Analysis Group, University of New Hampshire, Durham, New Hampshire, USA.

<sup>3</sup>Laboratoire d’Oceanographie Spatiale, Institut Francais de Recherche et d’Exploitation de la Mer, Plouzane, France.

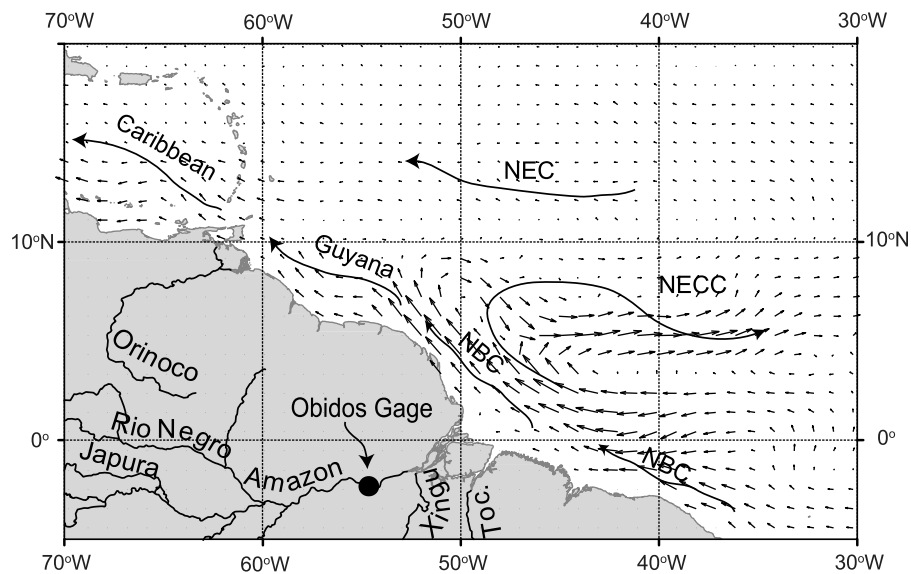


**Figure 1.** Area of interest: the northwestern Tropical Atlantic. On land, the Amazon River and its major tributaries within our region of interest are shown, as are the Orinoco, Xingu, and Tocantins (Toc.) rivers. The location of the Obidos, Brazil, discharge gauge is indicated as a solid circle. In the ocean, major currents are indicated: NBC, Northern Equatorial Current (NEC), NECC, Guyana Current, and Caribbean Current. The small flow vectors show the mean surface current direction and relative velocity during September. These were created from climatological Argo float trajectory data.

of the Amazon's water continues northwestward into the Guyana Current [Hellweger and Gordon, 2002], a sizable fraction reaching 3°N–10°N is carried eastward by the North Equatorial Counter Current (NECC) [Muller-Karger et al., 1989, 1995; Fratantoni and Glickson, 2002], which reaches maximal velocities during the boreal summer to fall period [Fonseca et al., 2004; Richardson and Reverdin, 1987]. Along the Brazilian shelf, up to 200 km offshore, the plume formed by the Amazon's discharge lies at the surface with a depth ranging from 3 to 10 m [Lentz and Limeburner, 1995]. Beyond the shelf, freshwater within the plume gradually attenuates with depth as it travels away from the source, with a penetration depth of 40 to 45 m as far as 2600 km offshore [Hellweger and Gordon, 2002; Hu et al., 2004]. Along with the freshwater, the Amazon provides the largest riverine flux of suspended (1200 Mt y<sup>-1</sup>) and dissolved matter (287 Mt y<sup>-1</sup>), which includes a dissolved organic matter (DOM) flux of 139 Mt y<sup>-1</sup> [Meybeck and Ragu, 1997]. These fluxes can have a dramatic effect on regional ecology as they represent potential subsidies of organic carbon, nutrients, and light attenuation into an otherwise oligotrophic environment [Muller-Karger et al., 1995].

[5] In the most proximal regions of the Amazon Plume, light attenuation by suspended detritus acts as the main limitation to phytoplankton growth [DeMaster et al., 1996]. Away from this region, as mineral detritus is removed by sinking, absorption attributable to organic substances begins to dominate the attenuation of light in surface waters. Del Vecchio and Subramaniam [2004] studied such conditions in the Amazon Plume and characterized the relative contributions of colored dissolved organic matter (CDOM), particulate organic material and phytoplankton to the total absorption field. Within their plume domain closest to shore

(between 6 and 8°N), absorption by CDOM accounted for the highest percentage of total constituent absorption. However, data from the offshore plume showed increasingly significant contributions of absorption by both phytoplankton and detritus more characteristic of the oligotrophic waters adjacent to the plume. This evidence points to conditions where fluxes of dissolved and particulate matter from the Amazon exert primary control on the underwater light field in the proximal regions of the plume. Yet in the more distal regions of the plume, attenuation that arises from phytoplankton activity becomes increasingly important.

[6] In the coastal ocean adjacent to river sources, CDOM tends to behave as a freshwater tracer, decreasing away from the river source with increasing salinity. A considerable range of CDOM values at river end-members have been reported [Blough and Del Vecchio, 2002], as the spatial variation of riverine CDOM is likely a function of regional hydrology and land cover attributes [Huang and Chen, 2009; Salisbury et al., 2008; Salisbury, 2003; Battin, 1998]. Nevertheless, linear correlations between coastal CDOM and salinity are well documented in ocean color literature, with reported relationships robust enough to allow salinity retrievals from CDOM and vice versa [e.g., Ferrari and Dowell, 1998; Palacios et al., 2009; D'Sa et al., 2002; Conny et al., 2009]. Linearity in the CDOM-salinity relationship implies conservative mixing dominated by two distinct end-members. Departures from linearity can occur when additional water masses are present [Blough and Del Vecchio, 2002] or by in situ subsidies of CDOM released via net phytoplankton growth [Nelson et al., 1998; Yamashita and Tanoue, 2004; Twardowski and Donaghay, 2001; D'Sa, 2008], microbial utilization [e.g., Moran et al., 1999; Obernosterer and Herndl, 2000], or photochemical oxidation [e.g., Miller and Zepp, 1995].

[7] In addition to its role as a tracer of freshwater in coastal waters, CDOM often contributes significantly to total light attenuation in the blue region of the spectrum where chlorophyll *a* also absorbs strongly. This can lead to large errors (typically overestimates) in ocean color retrievals of phytoplankton biomass [e.g., *Carder et al.*, 1991; *Muller-Karger et al.*, 1989; *Del Vecchio and Subramaniam*, 2004]. Because CDOM is part of the ocean DOM pool that varies regionally with salinity, there is also considerable interest in the use of CDOM to study the spatial and temporal mixing of DOM in coastal waters [*Vodacek et al.*, 1997; *Ferrari*, 2000]. Recent work has shown the potential of using in situ optical and satellite ocean color data toward this goal [*Del Castillo and Miller*, 2008; *Mannino et al.*, 2008].

[8] Until recently, studies relating satellite ocean color imagery to river plumes have been limited by the lack of a corresponding spatial mapping of near-surface salinity. In this work, the new salinity product derived from microwave brightness temperature data collected by Advanced Microwave Scanning Radiometer–Earth Observing System (AMSR-E) enables a novel examination of the coincident behavior of colored detrital matter absorption (acdm) and salinity over a large regional scale [*Reul et al.*, 2009]. Our study examines the nature of this relationship within the Western Tropical Atlantic, and also along the trajectory of the Amazon’s freshwater plume. We then use additional ocean color satellite data to explore observed departures from conservative mixing as the plume moves along the shelf and then into the open ocean.

## 2. Data and Methods

### 2.1. Study Region

[9] Our study domain in the Western Tropical Atlantic extends from 5°S to 20°N and 70°W to 30°W (Figure 1). River basins draining into the Atlantic Ocean at the mouth of the Amazon (1.5°S–0.5°N and 48.6°W–49.5°W) were identified using the global Simulated Topological Network (STN) river network [*Vörösmarty et al.*, 2000]. Besides the Amazon basin and its tributaries, this included discharge from the Tocantins River which enters the Atlantic Ocean in close proximity to the Amazon mouth at ~1.2°S, 48.6°W.

### 2.2. Discharge Data

[10] Concurrent discharge data at the region of the Amazon mouth were not available for the time period of the satellite records (2003–2007). Instead, we used WBM<sub>plus</sub> [*Wisser et al.*, 2010], an extension of a grid-based water balance and transport model [*Federer et al.*, 2003; *Rawlins et al.*, 2003; *Vörösmarty et al.*, 1998] to estimate discharge to the Amazon mouth. WBM<sub>plus</sub> is a fully coupled water balance and transport model that simulates the vertical water exchange between the land surface and the atmosphere and the horizontal water transport along a prescribed river network. The model was forced with a new gridded, global time series of daily air temperature and precipitation from the University of Delaware (<http://climate.geog.udel.edu/~climate/>). For this study the model was run at a spatial resolution of 0.5° and at a daily time step. Daily data were averaged to create monthly discharge.

[11] Model results were compared to the Obidos, Brazil, discharge gauge observations over the time period of avail-

able data (1928–1998). This gave us confidence that the model produces reliable discharge estimates for the entire Amazon watershed. (Root-mean-square error (RMS) of WBM<sub>plus</sub> model versus Obidos gauge data,  $\text{RMS}_{\text{model}} = 3.3 \times 10^4 \text{ m}^3 \text{ d}^{-1}$ . RMS of Amazon climatology (at Obidos) versus Obidos gauge data,  $\text{RMS}_{\text{model}} = 4.2 \times 10^4 \text{ m}^3 \text{ d}^{-1}$ .) The model may, in fact, be better for our purposes than data from the single Obidos gauge. The Obidos gauge is located 750 km from the ocean [*Perry et al.*, 1996] and does not account for discharge from the Xingu River, the Tocantins River, the Maicuru River, and other smaller rivers that when combined, provide at least 11% of the average annual discharge to the coast (<http://www.sage.wisc.edu/riverdata/>). Indeed, the combined annual discharge below the Obidos gauge is larger than the Mississippi River discharge, which ranks fifth globally. Furthermore, the characteristics of the hydrograph and timing of flow at, above, and below Obidos are different. For example, while the gauge at Obidos typically shows maximum discharge in May, the Tocantins and Xingu Rivers have discharge maxima occurring in February. For these reasons we believe the model delivers reliable information on the timing and magnitude of the freshwater flux to the ocean, and is preferable to data from a single gauge or its climatology.

### 2.3. AMSR-E Surface Salinity Estimates

[12] Monthly gridded estimates of sea surface salinity (SSS) were derived within our study area at 0.5° spatial resolution using daily data from the AMSR-E passive microwave sensor operating aboard the NASA Aqua satellite. This satellite also carries the Moderate Resolution Imaging Spectroradiometer (MODIS) sensor, whose ocean color data are used in this study. The data were produced from 2003 to 2007 based on the difference in vertically polarized ocean microwave brightness temperatures ( $T_{\text{BV}}$ ) between 6.9 and 10.7 GHz frequencies. The surface salinity retrieval method uses both AMSR-E and sea surface temperature satellite data sets as discussed by *Reul et al.* [2009]. Three modifications to the Reul et al. methods that were incorporated in this study were the refinement of the requisite AMSR-E  $T_{\text{BV}}$  atmospheric corrections, discontinued use of a final SSS minimization based on comparison to the *Klein and Swift* [1977] model for the dielectric constant of seawater, and an improved empirical estimator due mostly to a largely expanded satellite and in situ matchup data set.

[13] The native resolution of the AMSR-E measurements are 56–70 km and, because of land contamination issues, SSS estimates are not available within ~80 km of the coastline. The Aqua satellite passes over this region daily and the SSS estimate can be acquired in day or night and through significant amounts of atmospheric water vapor and clouds, though we do reject rain events. There are typically more than 20 rain-free estimates averaged within a given pixel to produce each monthly value. A conservative salinity uncertainty for these monthly data is  $\pm 1.0$  practical salinity unit (psu). This value is derived from comparisons with in situ and climatological data including shipboard measurements, Argo floats, PIRATA buoys, and the SSS climatology of *Reverdin et al.* [2007]. While *Reul et al.* [2009] cited an RMS difference of 1.5 psu using only 2003 satellite versus in situ comparisons, the method and comparison data set changes

**Table 1.** Satellite Data Products

Product	Units	Obtained From	Satellite/Sensor	Reference
Salinity	psu	Brightness temperature from <a href="http://www.ghcc.msfc.nasa.gov/">http://www.ghcc.msfc.nasa.gov/</a>	NASA Aqua/AMSR-E	<i>Reul et al.</i> [2009]
QAA acdm <sub>443</sub> , total nonwater absorption ( $a_{T443}$ ), and particle backscatter ( $b_{bp443}$ )	$m^{-1}$	Derived using radiance data from <a href="http://oceandata.sci.gsfc.nasa.gov">http://oceandata.sci.gsfc.nasa.gov</a>	NASA Aqua/MODIS	<i>Lee et al.</i> [2002]
NASA chl_gsm01, chlorophyll a concentration	$ug L^{-1}$	NASA Giovanni ( <a href="http://daac.gsfc.nasa.gov/giovanni/">http://daac.gsfc.nasa.gov/giovanni/</a> )	NASA Aqua/MODIS	<i>Maritorena and Siegel</i> [2005], <i>Maritorena et al.</i> [2002]
NASA adg_gsm01, absorption due to dissolved and detrital material at 443 nm	$m^{-1}$	NASA Giovanni ( <a href="http://daac.gsfc.nasa.gov/giovanni/">http://daac.gsfc.nasa.gov/giovanni/</a> )	NASA Aqua/MODIS	<i>Maritorena and Siegel</i> [2005], <i>Maritorena et al.</i> [2002]
VGPM	$mgC m^{-2} d^{-1}$	Oregon State University ( <a href="http://www.science.oregonstate.edu/ocean.productivity/">http://www.science.oregonstate.edu/ocean.productivity/</a> )	NASA Aqua/MODIS, SeaSTAR/SeaWiFS	<i>Behrenfeld and Falkowski</i> [1997]
CbPM	$mgC m^{-2} d^{-1}$	Oregon State University ( <a href="http://www.science.oregonstate.edu/ocean.productivity/">http://www.science.oregonstate.edu/ocean.productivity/</a> )	NASA Aqua/MODIS, SeaSTAR/SeaWiFS	<i>Behrenfeld et al.</i> [2005]

lead to our present observed difference of 1.0 psu over 2003–2007. As discussed by *Reul et al.* [2009], there are several remaining uncertainty sources in the measurements, SSS inversion method, and in situ data comparisons that collectively suggest that this number may ultimately be an upper, not lower, limit to the monthly AMSR-E SSS estimate error bound. Most importantly, the present level of AMSR-E uncertainty is more than sufficient to resolve the large SSS gradients encountered in the Amazon-influenced study region. These new salinity maps from the AMSR-E sensor are independent from MODIS ocean color sensor data and present new opportunities to use ocean color data to examine the mixing and biochemical transformations as the Amazon discharge spreads into the Atlantic.

#### 2.4. Ocean Color Data

[14] Ocean color satellite data corresponding in time and space to the AMSR-E data were obtained from the MODIS sensor. We used level 3 daily, 9 km resolution water leaving radiance data (six bands at 412, 443, 488, 531, 551, and 667 nm) from the NASA ocean color data distribution center (<http://oceandata.sci.gsfc.nasa.gov/MODISA/>). Radiance data were used to estimate the absorption coefficient of colored detrital matter at the reference wavelength 443 nm ( $acdm_{443}$ ) using the quasi-analytical algorithm (QAA) of *Lee et al.* [2002]. The daily  $acdm_{443}$  data were averaged by month and spatially binned to  $0.5^\circ$  to correspond with the gridded salinity product.

[15] We assume the radiance data meets or exceeds NASA's goal of  $\pm 5\%$  accuracy for MODIS as indicated by H. Gordon and K. Voss (MODIS normalized water-leaving radiance algorithm theoretical basis document (MOD 18) version 5, 2004, available at [http://modis.gsfc.nasa.gov/data/atbd/atbd\\_mod18.pdf](http://modis.gsfc.nasa.gov/data/atbd/atbd_mod18.pdf)). The  $acdm_{443}$  product includes absorption by both particulate detritus and CDOM. The particulate and dissolved terms are combined into a single product by nature of the fact that their absorption coefficient spectra are similar, making it difficult to distinguish between them using remotely sensed data [*Maritorena et al.*, 2002]. Their absorption spectra are commonly modeled as an exponentially decaying curve with spectral slope  $S$  defining

how rapidly absorption decreases with increasing wavelength. For this study, an  $S$  value of 0.017 was selected based on an average of pooled values for our image region that fell within a salinity range of 0–33.0 [*Del Castillo et al.*, 1999; *Blough and Del Vecchio*, 2002; *Odriozola et al.*, 2007]. The QAA  $acdm_{443}$  algorithm has been validated with field data in turbid waters and was shown to have a maximum error of 18%, which decreased considerably in clearer waters [*Lee et al.*, 2002]. Nevertheless, it is expected that errors in  $acdm_{443}$  could be considerably greater in waters with high sediment concentrations, or where erroneous atmospheric correction leads to underestimates of water-leaving radiance at the violet and blue wavelengths.

[16] Although satellite salinity and  $acdm_{443}$  data were used to track the spatial and temporal aspects of the low-salinity plume, we recognize that while these two properties are related via physical mixing, they are not necessarily related chemically. Various biological, geochemical, and photochemical processes can perturb conservative mixing of salinity and colored detrital matter (cdm). To examine processes as they relate to net production of cdm as the plume mixes into the open ocean, we processed total nonwater absorption ( $a_{T443}$ ) and particle backscatter ( $b_{bp443}$ ) using the QAA algorithm, and compared results with additional ocean color satellite products from various sources. These products included output from the Carbon-based Primary Productivity Model (CbPM) [*Behrenfeld et al.*, 2005], the Vertically Generalized Production Model (VGPM) [*Behrenfeld and Falkowski*, 1997], and the NASA (gsm01) absorption and chlorophyll products [*Maritorena et al.*, 2002; *Maritorena and Siegel*, 2005]. All additional data products were interpolated on to a  $0.5^\circ$  grid from their original 9 km resolution. Table 1 lists the satellite products, their sources, and relevant citations. Table 2 lists the correlation coefficients of linear regressions between satellite variables and AMSR-E salinity or gsm01 chlorophyll.

#### 2.5. Analyses

[17] We generated seasonal climatologies of salinity and  $acdm_{443}$  by averaging the monthly satellite data for 2003–2007. The seasons were established according to the clima-

**Table 2.** Correlation Coefficients  $r^2$  Between Monthly Satellite Data Subtended by Amazon Plume Trajectories

Satellite Variable	Salinity	chl_gsm01
acdm <sub>443</sub> (QAA)	0.53	0.58
CbPM	0.19	0.24
VGPM	0.62	0.64
chl_gsm01	0.63	1
a <sub>T443</sub> (QAA)	0.61	0.69
bbp <sub>443</sub> (QAA)	0.39	0.54
adg_gsm01	0.48	0.63

tological Amazon hydrograph at Obidos (1928–1998) as follows: low discharge (November–January), ascending hydrograph (February–April), high discharge (May–July), and descending hydrograph (August–October).

### 2.5.1. Plume Trajectories

[18] We identified low-salinity plume trajectories on each of the monthly salinity images by subjectively tracing the lowest salinity throughout the plume trajectory using ArcMap™ software. Trajectories originated from the Amazon mouth ( $\sim 0.6^\circ\text{N}$ ,  $49.1^\circ\text{W}$ ) and continued along the lowest-salinity axis until a salinity of  $\sim 36$  was encountered. Each monthly trajectory was objectively improved using a  $3 \times 3$  pixel minimum filter along the traced axis, whereby trajectory positions were relocated based on the lowest local salinities identified by the filter. The plume often bifurcates at  $\sim 3^\circ\text{N}$ – $12^\circ\text{N}$  during the summer, with one trajectory continuing to the northwest and the other retroflected to the east. This phenomenon was observed in situ by *Del Vecchio and Subramaniam* [2004]. In these cases, we chose to trace only the data following the direction of the lowest contiguous salinity.

### 2.5.2. Monthly Climatologies

[19] Monthly climatologies of salinity and acdm<sub>443</sub> along the trajectories were analyzed as a function of distance along the plume axis. The data were binned by distance from the Amazon's mouth ( $\sim 50$  km bin<sup>-1</sup>) and then averaged by bin over the years 2003–2007 to create monthly climatologies.

### 2.5.3. Time Series

[20] To create time series of salinity and acdm<sub>443</sub> for comparison with discharge, monthly satellite data were averaged over a region influenced by the Amazon corresponding to the same extent used in the 1997–2002 satellite plume study by *Hu et al.* [2004] ( $0^\circ\text{N}$ – $15^\circ\text{N}$ ,  $45^\circ\text{W}$ – $62^\circ\text{W}$ ). In addition, to investigate the temporal behavior of acdm<sub>443</sub> within the plume, we divided each of the monthly trajectories according to its distance from the Amazon mouth as follows: proximal section, 0–600 km; medial section, 600–1200 km, and distal section, 1200–1800 km. Satellite data within these sections were retrieved, averaged and plotted against time. Due to extensive cloud cover or algorithm failure in very turbid coastal waters, some acdm<sub>443</sub> data were missing from the proximal section time series. In cases where the trajectory was less than 1800 km, data for the distal sections extended from 1200 km to the maximum trajectory length.

### 2.5.4. Departures From Conservative Mixing

[21] The acdm<sub>443</sub> anomalies were derived as a difference from a least squares linear regression between salinity and acdm<sub>443</sub> for each month and for all data along the plume trajectories. The differences between each observation and

the corresponding regression line were calculated, averaged by 50 km bins, and plotted against distance along the trajectory. The locations of positive and negative anomalies were then compared with regions of high and low ocean color derived productivity (Table 1).

## 3. Results and Discussion

### 3.1. Regional Salinity and acdm<sub>443</sub> Patterns

[22] The generalized pattern of how salinity and acdm<sub>443</sub> respond to the dynamics of Amazon discharge and the seasonal evolution of surface currents is revealed in the seasonal climatologies of salinity and acdm<sub>443</sub> (Figure 2). Within the northwestern sector of the domain, the influence of the Orinoco River is visible in both the salinity and acdm<sub>443</sub> data. However, the main body of this work focuses on the behavior of salinity and acdm<sub>443</sub> specific to the Amazon Plume. The trajectory of the contiguous low-salinity plume to  $\sim 36$  psu is traced on each of the seasonal salinity climatologies. (Figure 2, left).

[23] A low-salinity plume emanating from the Amazon mouth is always present. Although visual inspection of Figure 2 shows seasonal variability in the spatial extent of the low-salinity plume, the most striking pattern is the manner in which the Amazon Plume responds to the NBC and NECC. From November to April (low flow and ascending periods), the plume is carried northwestward on the NBC. Through the summer and fall (high flow and descending periods) much of the plume is carried eastward as the seasonal NECC retroflexion strengthens. Distributions of acdm<sub>443</sub> track spatial patterns that are similar to salinity near the coast, but tend to deviate at the more distal regions of the low-salinity plume (Figure 2, right).

### 3.2. Time Series of Discharge and Averaged Regional Ocean Variables

[24] Figure 3 shows the temporal relationship between WBM<sub>plus</sub> modeled discharge and the satellite variables used in this study. For comparison, the discharge climatology at Obidos is included in Figure 3 (top). Monthly averaged salinity data for the region ranged between 35.2 and 35.9. Although net precipitation in this region follows an annual cycle caused by the migration of the Intertropical Convergence Zone, salinity variability throughout is largely driven by the dynamics of river flow [*Muller-Karger et al.*, 1989; *Dessier and Donguy*, 1994; *Foltz et al.*, 2004]. Average annual salinity maxima ( $35.7 \pm 0.1$ ) occurred from January to March. Salinity minima ( $35.3 \pm 0.1$ ) occurred during May–July in all years except 2004. Although the salinity data are not perfectly phased in opposition with Amazon discharge, regional salinity minima always occurred within 2 months of maximum discharge. As expected, greater lags were found between maximum Amazon discharge and salinity minima at sites in the Caribbean where salinity minima occur in October–November (e.g., near Barbados [*Hellweger and Gordon*, 2002]), at the Pilot Research Array in the Tropical Atlantic (PIRATA Buoy) located at  $8^\circ\text{N}$ ,  $38^\circ\text{W}$ , [*Foltz et al.*, 2004] and near Puerto Rico [*Froelich et al.*, 1978]. The timing of salinity minima in the northern region of our domain is also influenced by the discharge of the Orinoco, whose maximum discharge usually occurs in August [*Muller-Karger et al.*, 1989]. Observed lags between

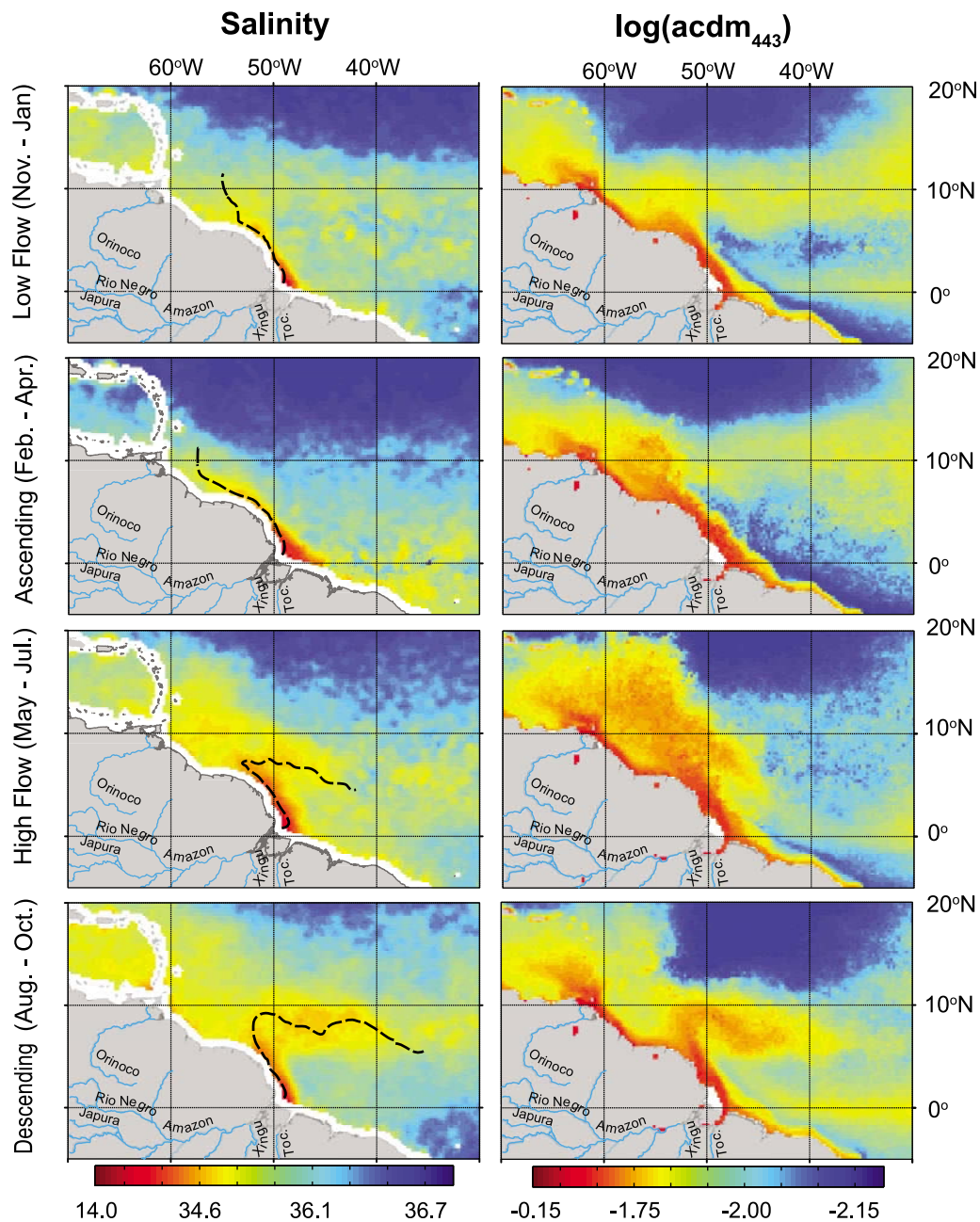


**Figure 2.** Seasonal climatologies (2003–2007) of satellite variables: (left) AMSR-E salinity and (right) MODIS  $\text{acdm}_{443}$ . The seasons (low flow, ascending, high flow, descending) were determined based on the climatological hydrograph of the Amazon River at Obidos, Brazil. Seasonal climatologies are estimated as the mean of seasonal NASA Aqua satellite data (2003–2007). Salinity is estimated using microwave brightness temperatures from the NASA AMSR-E sensor. Monthly  $\text{acdm}_{443}$  data are derived using monthly MODIS ocean color radiance data to which the QAA algorithm was applied (see text). The axis of the low-salinity plume climatology (to  $\sim 36$  psu) is traced on the salinity data (dashed black).

discharge and surface salinity are likely related to the time it takes river discharge to reach the observation regions [Hellweger and Gordon, 2002; Dessier and Donguy, 1994; Muller-Karger et al., 1989].

[25] Discharge and  $\text{acdm}_{443}$  are in phase, with  $\text{acdm}_{443}$  lagging discharge by 2–4 months (Figure 3, middle). The timing of the  $\text{acdm}_{443}$  (Figure 3, middle) is in approximate agreement with a time series (1997–2002) of satellite  $a_{\text{CDOM}}$  data reported for the same region [Hu et al., 2004]. Carbon-

based productivity (CbPM, Figure 3, bottom) is also in phase with discharge, and its maxima lag discharge by 1–2 months. During 2005–2007, CbPM was greater in magnitude than in 2003–2004. The change in the magnitude of annual CbPM is not explored in this work. Instead we use these data for a qualitative exploration of the potential causes of anomalies in conservative mixing of salinity and  $\text{acdm}_{443}$ .

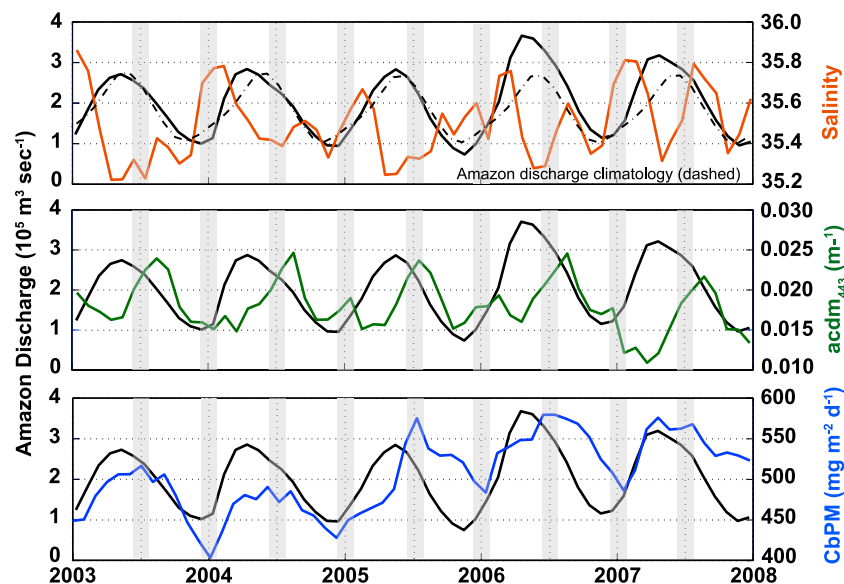


**Figure 3.** Time series of Amazon discharge and averaged regional satellite data. Modeled discharge from the Amazon (black), with climatological discharge at the Obidos gauge (dashed black, in Figure 3, top only). Monthly satellite data were averaged over the region  $0^{\circ}\text{N}$ – $15^{\circ}\text{N}$ ,  $45^{\circ}\text{W}$ – $62^{\circ}\text{W}$ . (top) AMSR-E salinity (red), (middle) absorption coefficient ( $\text{m}^{-1}$ ) of dissolved and detrital matter at 443 nm ( $\text{acdm}_{443}$ , green), and (bottom) carbon-based net primary productivity (CbPM, blue).

### 3.3. Tracking the Temporal Behavior of $\text{acdm}_{443}$ Within the Plume

[26] Variability of salinity and  $\text{acdm}_{443}$  in the coastal Western Tropical Atlantic is dominated by the Amazon's discharge. Indeed, when accounting for travel time, even over great distances, Amazon discharge is correlated with both salinity [Hellweger and Gordon, 2002] and ocean color [Hu *et al.*, 2004]. Hu *et al.* [2004] demonstrated that the absorption coefficient of satellite-retrieved CDOM was temporally correlated to discharge over a large area adjacent to the Amazon mouth. We ran similar analyses, but also exploited the spatially distributed AMSR-E salinity data to focus on the behavior of  $\text{acdm}_{443}$  specifically within the first 1800 km of the low-salinity plume (Figure 4).

[27] Figure 4 includes time series of modeled discharge (black), monthly average AMSR-E salinity (light brown) and  $\text{acdm}_{443}$  (green) for each plume section. We note that the modeled discharge at the Amazon mouth exceeds the climatological discharge at Obidos by an average of 11%, and that during the years 2006 and 2007 we estimate significantly higher discharge (see Figure 3, top). However, our estimates are consistent with June 2006 in situ observations reported for the Amazon Estuary by Rosario *et al.* [2009]. (For June 2006, Rosario *et al.* observation is  $301,562 \text{ m}^3 \text{ s}^{-1}$ ,  $\text{WBM}_{\text{plus}}$  estimate is  $332,385 \text{ m}^3 \text{ s}^{-1}$ , and Obidos climatology is  $244,158 \text{ m}^3 \text{ s}^{-1}$ .) Also included in Figure 4 are time series of the modeled flow for Rio Negro (black in Figure 4a, bottom only) and the regionally averaged  $\text{acdm}_{443}$  reported in Figure 3 (Figure 4c, green dashed).

[28] Table 3 shows correlation coefficients for regressions between discharge, salinity and  $\text{acdm}_{443}$  for each section of the plume. Included in Table 3 are correlation results in which discharge lagged the data by one month. For data within the proximal section (Figure 4a), salinity is phased in

opposition to discharge indicating the degree to which discharge influences regional surface salinity. The lag between highest discharge and lowest salinity (and vice versa) varies year by year by  $-2$  to  $+2$  months. This suggests the importance of physical processes other than discharge in driving regional surface salinity distributions. Figure 4a (bottom) suggests that the temporal pattern of  $\text{acdm}_{443}$  is also related to discharge. Temporal coherence between discharge and  $\text{acdm}_{443}$  can be logically interpreted as mixing of colored materials between high- and low-salinity end-members. However, the  $\text{acdm}_{443}$  curve is interesting in that, although its rise coincides with the rise of the hydrograph,  $\text{acdm}_{443}$  typically reached its maximum value 1–3 months after peak discharge. The cause of this is unclear. If  $\text{acdm}_{443}$  and surface salinity in the region were similarly driven by the Amazon's discharge, then we would expect both to have similar temporal dynamics (although opposite in sign). The lag implies a source of cdm that is entering the region during the descending limb of the hydrograph. Such a source could be of terrestrial or marine origin.

[29] A partial explanation of the lag could lie in the relative timing of flow from various Amazon source waters having differing optical properties. Tributaries of the Amazon are classically identified by their color depending on the predominance of dissolved organic matter (black water), suspended sediment (white water), or high phytoplankton production (clear water) [Devol and Hedges, 2001; Moreira-Turcq *et al.*, 2003]. Black water tributaries of the Amazon have high concentrations of dissolved humic substance [Mounier *et al.*, 1999] that would presumably provide an enhanced flux of CDOM. The black water tributary Rio Negro, contributes greater than 12% of the total Amazon discharge [Moreira-Turcq *et al.*, 2003] and is the world's largest black water river. Its maximum discharge occurs during June–August, approximately one month later than

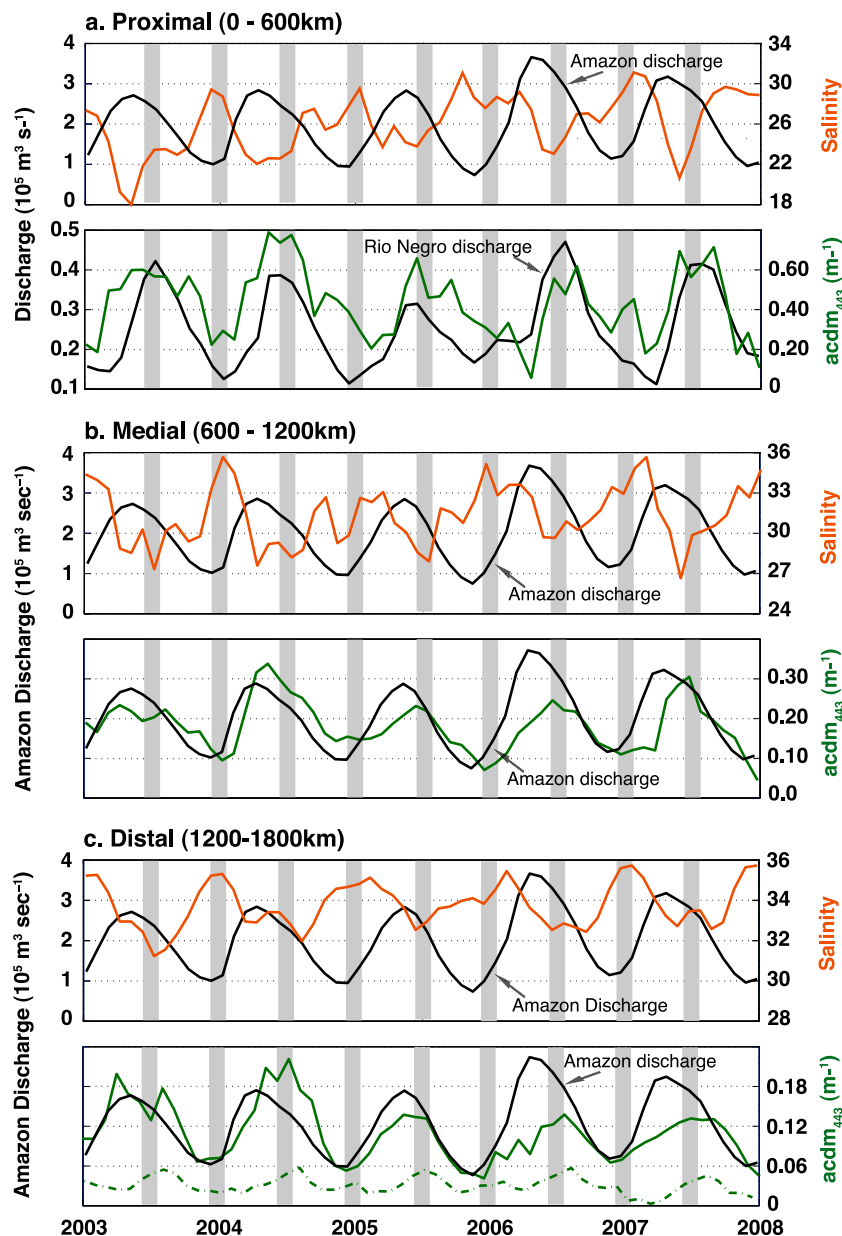


**Figure 4.** Time series of monthly salinity,  $\text{acdm}_{443}$  and discharge. Data were retrieved and averaged for locations corresponding to the proximal (mouth to 600 km), medial (600–1200 km), and distal (1200–1800 km) sections of the low-salinity plume trajectories and then plotted as a function of time. Salinity (red), modeled Amazon discharge (black), modeled discharge for the Rio Negro (black, in Figure 4a, bottom only),  $\text{acdm}_{443}$  (green), and averaged  $\text{acdm}_{443}$  for the same region as Figure 3 (dashed green). Note the different axis scales for each plot.

the maximum discharge downstream at Obidos (Figure 4a, bottom). The timing of the Amazon flood wave is largely controlled by the dynamics of the floodplain [Coe *et al.*, 2008], and its velocity is estimated to be  $<50 \text{ cm s}^{-1}$  [Richey *et al.*, 1989; Han *et al.*, 2009]. Assuming a mean velocity of  $50 \text{ cm s}^{-1}$ , it would take approximately one month for the maximum discharge of the Rio Negro to travel from its Amazon confluence ( $\sim 3.2^\circ\text{S}$ ,  $60.2^\circ\text{W}$ ) to the Amazon mouth, approximately 1400 km away. Thus the arrival time of maximum discharge from highly colored Rio Negro to the coast would more closely correspond to the

timing of maximum  $\text{acdm}_{443}$  that we observe within the proximal plume section.

[30] Alternatively, it is feasible that the draining of flooded lowlands (aka várzea lakes) during waning flow [Fisher and Parsley, 1979; Devol *et al.*, 1995] contributes to the observed lag between high discharge and high  $\text{acdm}_{443}$ . For example, in a tributary of the Orinoco River, Battin [1998] found that CDOM absorption increased as discharge decreased. Similar conditions were described by Mladenov *et al.* [2005] for the Okavango Delta, Botswana. In both cases the persistence of high absorption after peak discharge

**Table 3.** Correlation Coefficients for Discharge Versus  $acdm_{443}$  Along Amazon Plume Trajectory Sections<sup>a</sup>

	Proximal		Medial		Distal	
	$acdm_{443}$	Salinity	$Acdm_{443}$	Salinity	$acdm_{443}$	Salinity
Modeled Amazon Q, 0 lag	0.28	0.50	0.39	0.21	0.23	<i>0.06</i>
Modeled Rio Negro Q, 0 lag	0.45	0.32	0.37	0.46	0.20	0.45
Modeled Amazon Q, 1 lag	0.27	0.38	0.60	0.52	0.32	0.31
Modeled Rio Negro Q, 1 lag	0.34	<i>0.08</i>	0.14	0.22	<i>0.11</i>	0.43
Salinity	0.49	1.00	0.69	1.00	0.28	1.00

<sup>a</sup>Italics values are not significant at  $p < 0.001$ .

was attributed to the delayed draining of carbon-rich floodplain soils.

[31] It is also possible but less likely that estuarine and coastal processes providing seasonal subsidies of  $cdm$  could explain the lag between maximum discharge and  $acdm_{443}$ . Resuspension of organic particulates near the coast would increase organic detrital absorption ( $a_d$ ) and thus,  $acdm_{443}$ . The release of CDOM during resuspension events has been cited by several investigators [D'Sa, 2008; Conmy *et al.*, 2009; Boss *et al.*, 2001]. However, maximum wind stress and wave energy on the Amazon Shelf both occur during December–April [Geyer and Beardsley, 1995]. As such, the seasonality of conditions that would promote sediment resuspension do not support the idea that seasonal resuspension is the cause of the observed discharge- $acdm_{443}$  lag.

[32] Since the presence of biomass is often correlated with  $a_{CDOM}$  and  $a_d$ , [Nelson *et al.*, 1998; D'Sa, 2008; Chen and Gardner, 2004; Yamashita and Tanoue, 2004] it could be argued that  $cdm$  subsidies arising as a result of seasonal phytoplankton dynamics provides a partial explanation for the observed lag. On the Amazon Shelf encompassing the proximal section ( $\sim$ salinity less than 32), production is controlled by light availability, and its highest rates are measured where particulate loads settle [Smith and DeMaster, 1996; DeMaster and Aller, 2001]. The combination of low wave energy (May–October) and declining discharge may favor particle settling and thus provide sufficient irradiance for abundant phytoplankton growth coinciding with the timing of maximal  $acdm_{443}$ .

[33] In the medial plume section (Figure 4b, top), the seasonal coherence between salinity and discharge is weaker. Lower salinity coincided with maximum discharge in 2004, but lagged maximum discharge by 1–3 months in other years. At a reference surface current speed of  $50 \text{ cm s}^{-1}$  for the region [cf. Limeburner *et al.*, 1995; Johns *et al.*, 1998], Amazon discharge is expected to enter the medial section at approximately day 16 and leave at approximately day 32. Because of further dilution with oceanic waters, the  $acdm_{443}$  values in the medial section are much lower than in the proximal section (note different scales in Figure 4). Likewise, the annual change in magnitude of  $acdm_{443}$  in the medial section is only  $\sim 50\%$  that of the proximal section. Annual  $acdm_{443}$  maxima in the medial section typically occurred within a month of the maxima in the proximal section, perhaps reflecting the short travel time from the proximal to the medial section.

[34] The distal section can occupy a range of locations from the Guyana coast to oceanic waters more than 1000 km off the Brazilian coast (see Figure 2). Nevertheless, salinity at the varying distal locations follows a distinct annual cycle that has a range of 3–4.5 psu. Salinity minima lag discharge

by 1–4 months (Figure 4c). Assuming the surface current speed of  $50 \text{ cm s}^{-1}$ , Amazon water is expected to enter the distal section in approximately one month and occupy it for at least two weeks. The discrepancy between the estimated arrival time of Amazon Plume water and the observed salinity minima suggests the potential for other processes such as net precipitation or vertical mixing to influence the observed salinity. The temporal pattern of  $acdm_{443}$  is oppositely phased with salinity, and its maximal values lag discharge by 1–3 months in all years except 2005. Such a lag is consistent with satellite ocean color  $a_{CDOM}$  observations made by Hu *et al.* [2004]. However, relative to the timing of  $acdm_{443}$  in the proximal section,  $acdm_{443}$  maxima along the distal section either coincides with, or occurs  $\sim 1$  month earlier than  $acdm_{443}$  in the medial section. As with the other plume sections, the timing of maximum  $acdm_{443}$  within the distal section invokes the potential for perturbations to  $cdm$  not directly related to the hydrograph of the Amazon. Although  $acdm_{443}$  in the distal section is about 4 times smaller in magnitude than  $acdm_{443}$  in the proximal section, it is still far greater than the regional average reported in Figure 3 (cf. green dashed line, Figure 4c). Likewise salinity variability in the distal section is greater than that of the regional average (Figure 3). This highlights the fact that even at higher salinities, the Amazon is still a dominant influence on the salinity and absorption fields of the Western Tropical Atlantic.

### 3.4. The Spatial Distribution of $acdm$ Relative to Salinity Along the Plume Trajectory

[35] Monthly climatologies of salinity and  $acdm_{443}$  along the trajectories (Figure 5) show a prevailing pattern of increasing salinity corresponding to decreasing  $acdm_{443}$  as distance from the Amazon Mouth increases. However, there is considerable variability within the first 500 km of the plume, as salinity and  $acdm_{443}$  both change over short distances. Seaward of 300 km, there are many intervals of 50–200 km in which 0.5–2.0 psu changes in the magnitude of salinity parallel opposite changes in  $acdm_{443}$ , suggesting a strong linkage between the dynamics affecting both salinity and  $acdm_{443}$ . For example, beyond 500 km, notable decreases in salinity accompanied by increases in  $acdm_{443}$  are observed from July to November. Further along the trajectories smaller articulations in salinity elicit a small response in  $acdm_{443}$  (e.g., March through July at  $\sim 800$  km). Beyond 800 km, salinity gradually increases, usually corresponding to similar decreases in  $acdm_{443}$ . A notable exception is found during June where an increasing trend in  $acdm_{443}$  is observed beyond 1600 km.

[36] Pronounced seasonal patterns in the data are not readily apparent. However, during the low-flow period

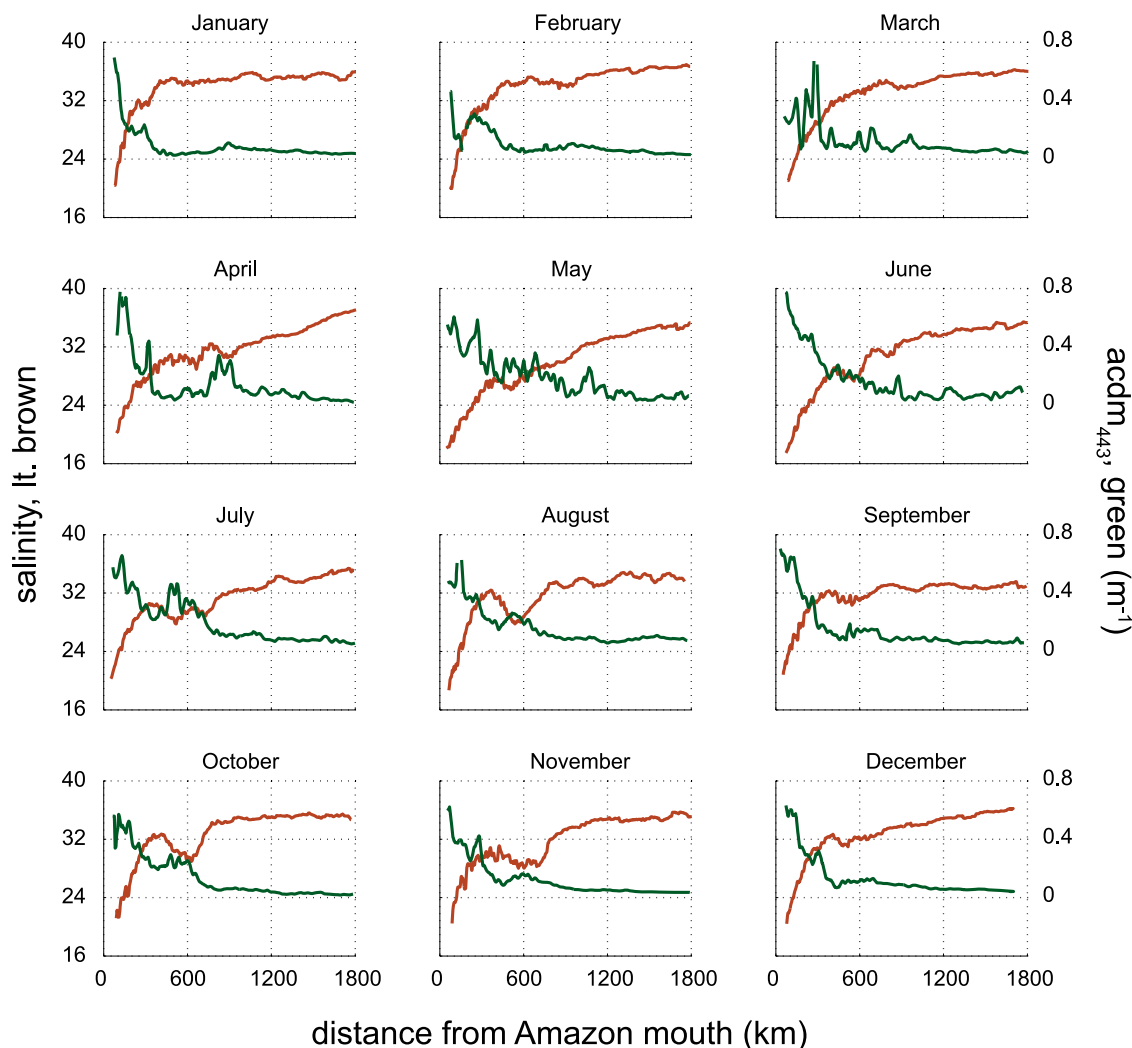


**Figure 5.** Monthly climatologies of salinity and  $acdm_{443}$  along the low-salinity plume trajectories (2003–2007). Salinity (red) and  $acdm_{443}$  (green). For each climatological month, all salinity and  $acdm_{443}$  data subtended by the low-salinity trajectories were binned by distance from the Amazon mouth ( $50 \text{ km bin}^{-1}$ ), averaged, and plotted as a function of distance.

(November–January) the pattern of salinity versus distance shows a sharper increase in the salinity over the first 500 km than in other seasons. This is contrasted by more gradual decreases during higher flow months (May–August). Such patterns are likely related to varying volumes of freshwater delivered and subsequently mixed during the Amazon’s hydrological regime. Another seasonal feature is the presence of a fresh water pool at 600–800 km that develops during the descending flow (August–October) and persists through November. Although explanation of this feature is beyond the scope of this effort, a possible mechanism in the Amazon Plume may be attributed to inshore upwelling of Bottom Boundary Layer Water, a phenomenon observed by Curtin [1986] during high-discharge periods.

### 3.5. Deviations From Conservative Salinity-cdm Mixing: potential Perturbations From Phytoplankton and Photo-oxidation

[37] Although it is clear the mixing of Amazon River water with the surrounding ocean explains much of the

$acdm_{443}$  signal for hundreds of kilometers along the plume, we find that there are notable anomalies in the conservative mixing of salinity and cdm. We examined anomalies of the linear salinity- $acdm_{443}$  relationship to explore, qualitatively, whether other coincident ocean products could shed light on their cause. First, we hypothesize that as Amazon Plume water ages there is a greater likelihood for the cdm pool to degrade via photochemical processes. We reason that distance from the Amazon source along the plume trajectory can be used as a simple proxy for the amount of time plume waters are exposed to solar irradiance. That is, waters farthest along the trajectory would be more susceptible to photo-oxidation and thus would show a higher occurrence of negative anomalies. We did not consider the seasonality of cloud cover or changes in day length that could alter the amount of light exposure. The blue curve in Figure 6a shows that data within the first 500 km is dominated by positive anomalies that decrease rapidly with distance. Beyond 500 km the anomalies are close to zero, but are predominately negative. Thus the anomaly distribution

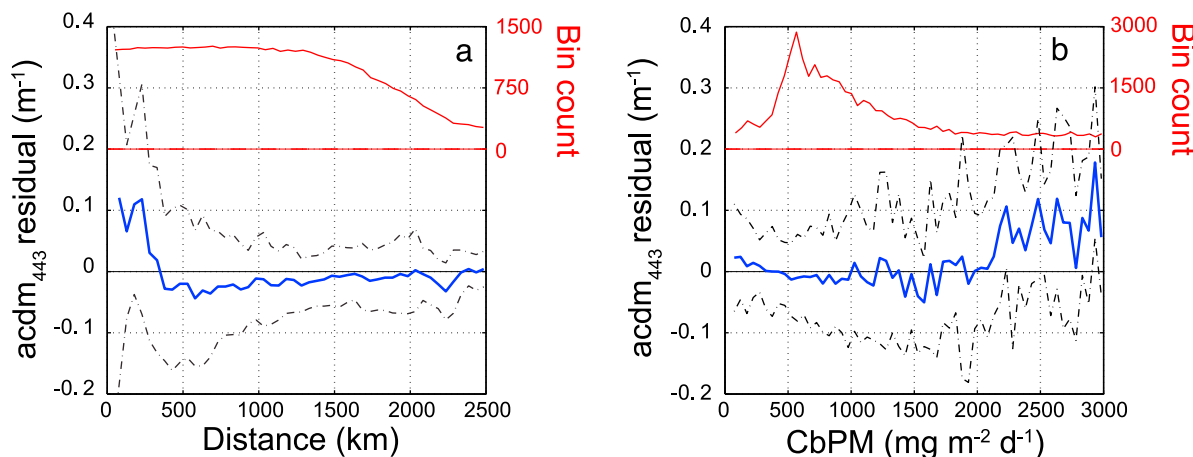


**Figure 6.** (a) Distance (km) versus  $\text{acdm}_{443}$  residual (blue). (b) Satellite CbPM data versus  $\text{acdm}_{443}$  residual (blue). Red lines represent the number of values in each bin, binned by 50 km intervals in Figure 6a and binned by 50  $\text{mgC m}^{-2} \text{d}^{-1}$  intervals in Figure 6b. The dashed lines represent  $\pm 1$  standard deviation of each bin average.

provides evidence for rapid light-mediated changes over the first 500 km, with much smaller changes occurring as the plume travels away from its source. Observations of multi-spectral fluorescence along the Orinoco Plume trajectory by *Del Castillo et al.* [1999] provide a reasonable analogy for our findings. *Del Castillo et al.* [1999] found that as distance from the plume source increased, a sharp decrease in the emission maxima of a fluorophore corresponding to fulvic and humic material was observed. It was further determined that the observed change was unrelated to conservative mixing. However, a secondary fluorophore under study did not change and was considered resistant to photodegradation. Thus, upon increased exposure to sunlight, photolabile material degraded rapidly, leaving photo-resistant material to persist as it traveled with the plume.

[38] We further hypothesize that positive anomalies will be more likely to be associated with the production and subsequent remineralization of phytoplankton. This is because production of phytoplankton biomass increases light attenuation by organic particles [*Fennel and Boss, 2003; Behrenfeld and Boss, 2006*] and also because in situ remineralization of biomass can increase  $a_{\text{CDOM}}$  [*Nelson et al., 1998; Yamashita and Tanoue, 2004; Boss et al., 2001; Twardowski and Donaghay, 2001*].

[39] We examined satellite-derived primary productivity with the thought that these products could be used as a proxy for the rate of biomass accumulation [cf. *Muller-Karger et al., 2005*]. A premise of the VGPM and other chlorophyll-based models is that productivity varies predictably with chlorophyll [*Behrenfeld and Falkowski, 1997*]. Indeed, correlations between satellite chlorophyll and VGPM data, and also between VGPM and salinity, were high for our study (Table 2). Similar correlations using the CbPM productivity data were considerably lower. A distinction between the two productivity products is that the CbPM estimates are strongly influenced by satellite derived particulate backscatter and phytoplankton absorption coefficients [*Garver and Siegel, 1997; Maritorea et al., 2002; Siegel et al., 2002*] while the VGPM is dominated by satellite chlorophyll [*Behrenfeld and Falkowski, 1997*].

Because of its lower correlation with both salinity and chlorophyll, we chose the CbPM data to study potential anomalies in conservative salinity- $\text{acdm}_{443}$  mixing caused by phytoplankton activity. Inherent in this choice is the assumption that CbPM data are sufficiently accurate to capture monthly productivity variability over the spatial domain of the trajectories.

[40] CbPM estimates were binned and averaged by 50  $\text{mg m}^{-2} \text{d}^{-1}$  increments. The blue curve in Figure 6b shows  $\text{acdm}_{443}$  anomalies (averaged for each bin) plotted across CbPM data ranging from 100 to 3000  $\text{mg m}^{-2} \text{d}^{-1}$ . This interval contains ~96% of the data. Slight negative anomalies predominate at productivity values below 750  $\text{mg m}^{-2} \text{d}^{-1}$  where 71% of the data occur. This is followed by an interval in which considerable variability is observed (750–1600  $\text{mg m}^{-2} \text{d}^{-1}$ ), which in turn is followed by an interval showing an increasing trend of positive anomalies. We note that data above 1600  $\text{mg m}^{-2} \text{d}^{-1}$  account for 12% of the data set. At productivity values >750  $\text{mg m}^{-2} \text{d}^{-1}$ , the association of phytoplankton production with the positive anomalies supports our hypothesis for phytoplankton-derived subsidies of  $a_d$  and  $a_{\text{CDOM}}$ . An alternative explanation for this association could be lateral or subsurface mixing of a third end-member with higher  $\text{acdm}_{443}$ . The Orinoco River is a candidate end-member for lateral mixing. However, the trajectory of the Orinoco is such that it would rarely interfere with our analyses along the Amazon trajectory [see *Muller-Karger et al., 1989*] (see also Figure 2). Neither is it likely that mixing from a subsurface end-member could cause positive anomalies, since reported  $a_{\text{CDOM}}$  values are quite low in water beneath the Amazon Plume [*Del Vecchio and Subramaniam, 2004*]. (In Amazon Plume waters,  $a_{\text{CDOM}}$  (at 355 nm) was always  $< 0.15 \text{ m}^{-1}$  for depths greater than 30 m.)

[41] The presence of viable phytoplankton communities in plume regions that are presumed to be nutrient limited is somewhat problematic. However, there is ample field evidence of abundant phytoplankton growth in all but the most turbid sections of the Amazon Plume [*Hulburt and Corwin, 1969; DeMaster et al., 1996; Shipe et al., 2006; Subramaniam et al., 2008*]. Mechanisms that could supply

nutrients necessary to support phytoplankton growth include in situ remineralization of biomass [Morell and Corredor, 2001; Muller-Karger et al., 1995], remineralization of dissolved organic matter [Morell and Corredor, 2001], nitrogen fixation by diazotrophs [Subramaniam et al., 2008], and nutrient pumping via eddy upwelling [Longhurst, 1993]. In the plume regions detached from the coast, Del Vecchio and Subramaniam [2004] observed that  $a_d$  provided a higher proportion of the total absorption field, than it did in the more proximal regions. In this work the authors reported that the  $a_d$  was largely derived from in situ phytoplankton sources. It is also possible that phytoplankton could be advected from regions more replete with nutrients [Muller-Karger et al., 1995]. Muller-Karger et al. [1988, 1995] speculated that away from the coast, Amazon Plume waters likely contained CDOM and phytoplankton, and that each contributed to the plume's color. Additional evidence for the association of  $acdm_{443}$  and phytoplankton productivity can be found in Figure 3c. For each year the maximum averaged CbPM values over the region either coincide with, or precede the maximum  $acdm_{443}$  values. Within the same extent, Hu et al. [2004] showed that maximum satellite chlorophyll values were in phase with maximum satellite  $a_{CDOM}$  values, and during 4 out of 6 years, chlorophyll maxima preceded  $a_{CDOM}$  maxima by 1 month. Thus the temporal dynamics of both satellite proxies for phytoplankton demonstrate the potential for biomass or its subsequent remineralization to contribute to the observed positive anomalies.

#### 4. Summary and Conclusions

[42] We report on a 5 year time series of satellite variables over a broad region of the Western Equatorial Atlantic that receives the Amazon's discharge. AMSR-E salinity data enabled the first spatiotemporal analyses of  $acdm_{443}$  relative to salinity. Our results clearly demonstrate spatial coherence between salinity and  $acdm_{443}$  in plume-influenced waters at monthly and seasonal time scales. Deviations from conservative mixing point to processes that contribute or remove colored detrital matter, as measured by proxy as  $acdm_{443}$ , along the plume. Time series of modeled discharge at the Amazon mouth corresponded to local salinity minima (April–July) and  $acdm_{443}$  maxima (July–August). However, salinity minima within the first 600 km of the Amazon Plume trajectory preceded  $acdm_{443}$  maxima by 0–3 months. We submit that a partial explanation for this observed lag is due to the flux of colored water from the large Rio Negro tributary, whose peak discharge typically occurs in June. Farther offshore and along the plume trajectory from 600 to 1200 km, temporal patterns of salinity and  $acdm_{443}$  are similar to the proximal region, albeit of different magnitudes. At the distal section of the plume (beyond 1200 km) the timing of maximal  $acdm_{443}$  varied by 1 month, often preceding the timing of maximal  $acdm_{443}$  at the Amazon mouth. Timing of maximal  $acdm_{443}$  over the entire study region was similar to that of  $a_{CDOM}$  observed by Hu et al. [2004]. In turn, the maximal  $acdm_{443}$  averaged over the entire region was always within a month of that in the distal plume section.

[43] There was evidence for local sources and sinks of  $acdm_{443}$  along the plume trajectory and over the broader region. Anomalies to a linear mixing relationship between

$acdm_{443}$  and salinity along the plume trajectory were evaluated versus distance from the plume, with anomalies becoming increasingly negative with distance. We interpret this as evidence suggesting photo-oxidation and loss of  $acdm_{443}$  as the plume ages. The concept of distance as proxy for irradiance exposure time and the tendency for  $acdm_{443}$  to undergo photochemical degradation along a plume trajectory requires additional consideration. The anomalies were also compared to satellite derived primary productivity, with higher productivity corresponding to positive anomalies. This finding supports those by Del Vecchio and Subramaniam [2004] who reported an increased proportion of detrital absorption within the higher salinity regions of the Amazon Plume. We expect that these loss and production processes occur simultaneously in the plume and that one may often locally dominate the observed anomaly. Future work will focus on combining simple process-based models with these and other satellite data to better quantify their relative contributions.

[44] These new satellite observations support the concept that the Amazon River discharge governs surface light absorption over a large area in the Equatorial Atlantic. Moreover, the observed time series of averaged salinity and  $acdm_{443}$  at the proximal, medial and distal reaches invoke questions regarding the relative timing of  $acdm_{443}$  along the plume trajectory. Within the proximal section, what is the cause for the annually repeating lag in the maximum  $acdm_{443}$  with respect to the month of maximum river discharge? Within the medial and distal reaches, why does the timing of  $acdm_{443}$  maxima differ from, or even precede, maxima in the  $acdm_{443}$  nearest to the Amazon source? Analysis of satellite productivity data coincident with  $acdm_{443}$  brings into play the importance of phytoplankton activity as subsidies of the detrital or dissolved components of  $acdm_{443}$ . Although further analysis of the processes contributing to  $acdm_{443}$  source and sink terms is possible with these data, more rigorous characterization of these processes could be informed with in situ analyses of  $acdm_{443}$  transformations within the plume guided by near real time satellite monitoring of plume advection along the coast and off the shelf. Certainly sampling efforts aimed at monitoring the optical properties at the Amazon end-member also remain a priority.

[45] **Acknowledgments.** We are grateful for the NASA support that funded our efforts: NASA Carbon grants (NNX08AL80G and NNX08AE59G), NASA Ocean Salinity Team grant (NNX09AU69G), and NASA NEWS (NNX09AU89G). We deeply appreciate the technical support and scholarly advice from colleagues Tim Moore and Stanley Glidden. Observed discharge data has been provided by the Global Runoff Data Centre (GRDC) in Koblenz, Germany. We appreciate the insights offered by two anonymous reviewers and our primary editor, Miguel Goni.

#### References

- Battin, T. J. (1998), Dissolved organic matter and its optical properties in a blackwater tributary of the Upper Orinoco, Venezuela, *Org. Geochem.*, 28, 561–569, doi:10.1016/S0146-6380(98)00028-X.
- Behrenfeld, M. J., and E. Boss (2006), Beam attenuation and chlorophyll concentration as alternative optical indices of phytoplankton biomass, *J. Mar. Res.*, 64, 431–451, doi:10.1357/002224006778189563.
- Behrenfeld, M. J., and P. G. Falkowski (1997), Photosynthetic rates derived from satellite-based chlorophyll concentration, *Limnol. Oceanogr.*, 42, 1–20, doi:10.4319/lo.1997.42.1.0001.

- Behrenfeld, M. J., E. Boss, D. A. Siegel, and D. M. Shea (2005), Carbon-based ocean productivity and phytoplankton physiology from space, *Global Biogeochem. Cycles*, *19*, GB1006, doi:10.1029/2004GB002299.
- Blough, N. V., and R. Del Vecchio (2002), Chromophoric DOM in the coastal environment, in *Biogeochemistry of Marine Dissolved Organic Matter*, edited by D. A. Hansell and C. A. Carlson, pp. 509–546, Academic, San Diego, Calif., doi:10.1016/B978-012323841-2/50012-9.
- Boss, E., W. S. Pegau, Z. N. V. Zaneveld, and H. Barnard (2001), Spatial and temporal variability of absorption by dissolved material at a continental shelf, *J. Geophys. Res.*, *106*, 9499–9507, doi:10.1029/2000JC900008.
- Carder, K. L., S. K. Hawes, K. A. Baker, R. C. Smith, R. G. Steward, and B. G. Mitchell (1991), Reflectance model for quantifying chlorophyll a in the presence of productivity degradation products, *J. Geophys. Res.*, *96*, 20,599–611, doi:10.1029/91JC02117.
- Chen, R. F., and G. B. Gardner (2004), High-resolution measurements of chromophoric dissolved organic matter in the Mississippi and Atchafalaya River Plume regions, *Mar. Chem.*, *89*, 103–125, doi:10.1016/j.marchem.2004.02.026.
- Coe, M. T., M. H. Costa, and E. A. Howard (2008), Simulating the surface waters of the Amazon River basin: Impacts of new river geomorphic and flow parameterizations, *Hydrol. Processes*, *22*, 2542–2553, doi:10.1002/hyp.6850.
- Conmy, R. N., P. G. Coble, J. P. Cannizzaro, and C. A. Heil (2009), Influence of extreme storm events on West Florida Shelf CDOM distributions, *J. Geophys. Res.*, *114*, G00F04, doi:10.1029/2009JG000981.
- Curtin, T. B. (1986), Physical observations in the plume region of the Amazon River during peak discharge: Part II. Water masses, *Cont. Shelf Res.*, *6*, 53–71, doi:10.1016/0278-4343(86)90053-1.
- Del Castillo, C. E., and R. L. Miller (2008), On the use of ocean color remote sensing to measure the transport of dissolved organic carbon by the Mississippi River Plume, *Remote Sens. Environ.*, *112*, 836–844, doi:10.1016/j.rse.2007.06.015.
- Del Castillo, C. E. D., P. G. Coble, J. M. Morell, J. Lopez, and J. Corredor (1999), Analysis of the optical properties of the Orinoco River Plume by absorption and fluorescence spectroscopy, *Mar. Chem.*, *66*, 35–51, doi:10.1016/S0304-4203(99)00023-7.
- Del Vecchio, R., and A. Subramaniam (2004), Influence of the Amazon River on the surface optical properties of the Western Tropical North Atlantic Ocean, *J. Geophys. Res.*, *109*, C11001, doi:10.1029/2004JC002503.
- DeMaster, D. J., and R. C. Aller (2001), Biogeochemical processes on the Amazon shelf: Changes in dissolved and particulate fluxes during river/ocean mixing, in *The Biogeochemistry of the Amazon Basin*, edited by M. E. McClain, R. L. Victoria, and J. E. Richey, pp. 328–357, Oxford Univ. Press, New York.
- DeMaster, D. J., W. Smith, D. M. Nelson, and J. Y. Aller (1996), Biogeochemical processes in Amazon shelf waters: Chemical distributions and uptake rates of silicon, carbon and nitrogen, *Cont. Shelf Res.*, *16*, 617–643, doi:10.1016/0278-4343(95)00048-8.
- Dessier, A., and J. R. Donguy (1994), The sea surface salinity in the tropical Atlantic between 10°S and 30°N: Seasonal and interannual variations (1977–1989), *Deep Sea Res. Part I*, *41*, 81–100, doi:10.1016/0967-0637(94)90027-2.
- Devol, A. H., and J. I. Hedges (2001), Organic matter and nutrients in the main stem Amazon River, in *The Biogeochemistry of the Amazon Basin*, edited by M. E. McClain, R. L. Victoria, and J. E. Richey, pp. 275–306, Oxford Univ. Press, New York.
- Devol, A. H., B. R. Forsberg, J. E. Richey, and T. P. Pimentel (1995), Seasonal variation in chemical distributions in the Amazon River: A multi-year time series, *Global Biogeochem. Cycles*, *9*, 307–328, doi:10.1029/95GB01145.
- D'Sa, E. J. (2008), Colored dissolved organic matter in coastal waters influenced by the Atchafalaya River, USA: Effects of an algal bloom, *J. Appl. Remote Sens.*, *2*, 023502, doi:10.1117/1.2838253.
- D'Sa, E. J., C. Hu, F. E. Muller-Karger, and K. L. Carder (2002), Estimation of colored dissolved organic matter and salinity fields in case 2 waters using SeaWiFS: Examples from Florida Bay and Florida Shelf, *J. Earth Syst. Sci.*, *111*, 197–207, doi:10.1007/BF02701966.
- Federer, C. A., C. J. Vörösmarty, and B. Fekete (2003), Sensitivity of annual evaporation to soil and root properties in two models of contrasting complexity, *J. Hydrometeorol.*, *4*, 1276–1290, doi:10.1175/1525-7541(2003)004<1276:SOAETS>2.0.CO;2.
- Fennel, K., and E. Boss (2003), Subsurface maxima of phytoplankton and chlorophyll: Steady state solutions from a simple model, *Limnol. Oceanogr.*, *48*, 1521–1534, doi:10.4319/lo.2003.48.4.1521.
- Ferrari, G. M. (2000), The relationship between chromophoric dissolved organic matter and dissolved organic carbon in the European Atlantic coastal area and in the west Mediterranean Sea (Gulf of Lions), *Mar. Chem.*, *70*, 339–357, doi:10.1016/S0304-4203(00)00036-0.
- Ferrari, G. M., and M. D. Dowell (1998), CDOM absorption characteristics with relation to fluorescence and salinity in coastal areas of the southern Baltic Sea, *Estuarine Coastal Shelf Sci.*, *47*, 91–105, doi:10.1006/ecs.1997.0309.
- Fisher, T. R., and P. E. Parsley (1979), Amazon lakes: Water storage and nutrient stripping by algae, *Limnol. Oceanogr.*, *24*, 547–553, doi:10.4319/lo.1979.24.3.0547.
- Foltz, G., S. A. Grodsky, J. A. Carton, and M. McPhaden (2004), Seasonal salt budget of the northwestern tropical Atlantic Ocean along 38°W, *J. Geophys. Res.*, *109*, C03052, doi:10.1029/2003JC002111.
- Fonseca, C. A., G. J. Goni, W. E. Johns, and E. J. Campos (2004), Investigation of the North Brazil Current retroflection and North Equatorial Countercurrent variability, *Geophys. Res. Lett.*, *31*, L21304, doi:10.1029/2004GL020054.
- Fratantoni, D. M., and D. A. Glickson (2002), North Brazil Current ring generation and evolution observed with SeaWiFS, *J. Phys. Oceanogr.*, *32*, 1058–1074, doi:10.1175/1520-0485(2002)032<1058:NBCRG>2.0.CO;2.
- Froelich, N., D. K. Atwood, and G. S. Giese (1978), Influence of Amazon River discharge on surface salinity and dissolved silicate concentrations in the Caribbean Sea, *Deep Sea Res.*, *25*, 735–744, doi:10.1016/0146-6291(78)90627-6.
- Garver, S. A., and D. A. Siegel (1997), Inherent optical property inversion of ocean color spectra and its biogeochemical interpretation: 1. Time series from the Sargasso Sea, *J. Geophys. Res.*, *102*, 18,607–18,625, doi:10.1029/96JC03243.
- Geyer, W. R., and R. C. Beardsley (1995), Introduction to special section on physical oceanography of the Amazon Shelf, *J. Geophys. Res.*, *100*, 2281–2282, doi:10.1029/94JC03130.
- Han, S.-C., H. Kim, H. I.-Y. Yeo, P. Yeh, T. Oki, K.-W. Seo, D. Alsdorf, and S. B. Luthcke (2009), Dynamics of surface water storage in the Amazon inferred from measurements of inter-satellite distance change, *Geophys. Res. Lett.*, *36*, L09403, doi:10.1029/2009GL037910.
- Hellweger, F. L., and A. L. Gordon (2002), Tracing Amazon River water into the Caribbean Sea, *J. Mar. Res.*, *60*, 537–549, doi:10.1357/002224002762324202.
- Hickey, B. M., et al. (2010), River influences on shelf ecosystems: Introduction and synthesis, *J. Geophys. Res.*, *115*, C00B17, doi:10.1029/2009JC005452.
- Hu, C., E. T. Montgomery, R. W. Schmitt, and F. E. Muller-Karger (2004), The dispersal of the Amazon and Orinoco River water in the tropical Atlantic and Caribbean Sea: Observation from space and S-PALACE floats, *Deep Sea Res. Part II*, *51*, 1151–1171.
- Huang, W., and R. F. Chen (2009), Sources and transformations of chromophoric dissolved organic matter in the Neponset River Watershed, *J. Geophys. Res.*, *114*, G00F05, doi:10.1029/2009JG000976.
- Hulbert, E. M., and N. Corwin (1969), Influence of the Amazon River outflow on the ecology of the western tropical Atlantic. Part III. The planktonic flora between the Amazon River and the Windward Islands, *J. Mar. Res.*, *27*, 55–72.
- Johns, W. E., T. Lee, R. C. Beardsley, J. Candela, R. Limeburner, and B. M. Castro (1998), Annual cycle and variability of the North Brazil Current, *J. Phys. Oceanogr.*, *28*, 103–128, doi:10.1175/1520-0485(1998)028<0103:ACAVOT>2.0.CO;2.
- Klein, L. A., and C. T. Swift (1977), An improved model for the dielectric constant of sea water at microwave frequencies, *IEEE Trans. Antennas Propag.*, *25*, 104–111, doi:10.1109/TAP.1977.1141539.
- Lee, Z., K. L. Carder, and R. A. Arnone (2002), Deriving inherent optical properties from water color: A multiband quasi-analytical algorithm for optically deep waters, *Appl. Opt.*, *41*, 5755–5772, doi:10.1364/AO.41.005755.
- Lentz, S. J. (1995), Seasonal variations in the horizontal structure of the Amazon Plume inferred from historical hydrographic data, *J. Geophys. Res.*, *100*, 2391–2400, doi:10.1029/94JC01847.
- Lentz, S. J., and R. Limeburner (1995), The Amazon River Plume during AMASSEDs: Spatial characteristics and salinity variability, *J. Geophys. Res.*, *100*, 2355–2375, doi:10.1029/94JC01411.
- Limeburner, R., R. C. Beardsley, I. D. Soares, S. J. Lentz, and J. Candela (1995), Lagrangian flow observations of the Amazon River discharge into the North Atlantic, *J. Geophys. Res.*, *100*, 2401–2415, doi:10.1029/94JC03223.
- Longhurst, A. (1993), Seasonal cooling and blooming in tropical oceans, *Deep Sea Res.*, *40*, 2145–2165, doi:10.1016/0967-0637(93)90095-K.
- Longhurst, A. (1995), Interpreting CZCS images of the Amazon Plume, *Deep Sea Res. Part I*, *42*, 2139–2141, doi:10.1016/0967-0637(95)00086-0.
- Mannino, A., M. E. Russ, and S. B. Hooker (2008), Algorithm development and validation for satellite-derived distributions of DOC and

- CDOM in the U.S. Middle Atlantic Bight, *J. Geophys. Res.*, *113*, C07051, doi:10.1029/2007JC004493.
- Maritorena, S., and D. A. Siegel (2005), Consistent merging of satellite ocean color data sets using a bio-optical model, *Remote Sens. Environ.*, *94*, 429–440, doi:10.1016/j.rse.2004.08.014.
- Maritorena, S., D. A. Siegel, and A. Peterson (2002), Optimization of a semi-analytical ocean color model for global scale applications, *Appl. Opt.*, *41*, 2705–2714, doi:10.1364/AO.41.002705.
- McKee, B. A., R. C. Aller, M. A. Allison, T. S. Bianchi, and G. C. Kineke (2004), Transport and transformation of dissolved and particulate materials on continental margins influenced by major rivers: Benthic boundary layer and seabed processes, *Cont. Shelf Res.*, *24*, 899–926, doi:10.1016/j.csr.2004.02.009.
- Meybeck, M., and A. Ragu (1997), River discharges to the oceans: An assessment of suspended solids, major ions, and nutrients, *IAHS Publ.*, *243*, 1–245.
- Miller, R., and R. G. Zepp (1995), Photochemical production of dissolved inorganic carbon from terrestrial organic matter: Significance to the oceanic organic carbon cycle, *Geophys. Res. Lett.*, *22*, 417–420, doi:10.1029/94GL03344.
- Mladenov, N., D. M. McKnight, P. Wolski, and L. Ramberg (2005), Effects of the annual flood on dissolved organic carbon dynamics in the Okavango Delta, Botswana, *Wetlands*, *25*, 622–638, doi:10.1672/0277-5212(2005)025[0622:EOAFOD]2.0.CO;2.
- Moran, M. A., W. M. Sheldon, and J. E. Sheldon (1999), Biodegradation of riverine dissolved organic carbon in five estuaries of the southeastern United States, *Estuaries*, *22*, 55–64, doi:10.2307/1352927.
- Moreira-Turcq, P., P. Seyler, J. L. Guyot, and H. Etcheber (2003), Exportation of organic carbon from the Amazon River and its main tributaries, *Hydrol. Processes*, *17*, 1329–1344, doi:10.1002/hyp.1287.
- Morell, J. M., and J. E. Corredor (2001), Photomineralization of fluorescent dissolved organic matter in the Orinoco River Plume: Estimation of ammonium release, *J. Geophys. Res.*, *106*, 16,807–16,813, doi:10.1029/1999JC000268.
- Mounier, S., R. Braucher, and J. Y. Benaïm (1999), Differentiation of organic matter's properties of the Rio Negro basin by crossflow ultra-filtration and UV spectrofluorescence, *Water Res.*, *33*, 2363–2373, doi:10.1016/S0043-1354(98)00456-4.
- Muller-Karger, F. E., C. R. McClain, and P. L. Richardson (1988), The dispersal of the Amazon's water, *Nature*, *333*, 56–59, doi:10.1038/333056a0.
- Muller-Karger, F. E., C. R. McClain, T. R. Fisher, W. E. Esaias, and R. Varela (1989), Pigment distribution in the Caribbean Sea: Observations from space, *Prog. Oceanogr.*, *23*, 23–64, doi:10.1016/0079-6611(89)90024-4.
- Muller-Karger, F. E., P. L. Richardson, and D. McGillicuddy (1995), On the offshore dispersal of the Amazon's Plume in the North Atlantic, *Deep Sea Res. Part I*, *42*, 2127–2137, doi:10.1016/0967-0637(95)00085-2.
- Muller-Karger, F. E., R. Varela, R. Thunell, R. Luerssen, C. Hu, and J. J. Walsh (2005), The importance of continental margins in the global carbon cycle, *Geophys. Res. Lett.*, *32*, L01602, doi:10.1029/2004GL021346.
- Nelson, N. B., D. A. Siegel, and A. F. Michaels (1998), Seasonal dynamics of colored dissolved material in the Sargasso Sea, *Deep Sea Res. Part I*, *45*, 931–957, doi:10.1016/S0967-0637(97)00106-4.
- Obernosterer, I., and G. J. Herndl (2000), Differences in the optical and biological reactivity of the humic and non-humic DOC component in two contrasting coastal marine environments, *Limnol. Oceanogr.*, *45*, 1120–1129, doi:10.4319/lo.2000.45.5.1120.
- Odrozola, A. L., R. Varela, C. Hu, Y. Astor, L. Lorenzoni, and F. E. Muller-Karger (2007), On the absorption of light in the Orinoco River Plume, *Cont. Shelf Res.*, *27*, 1447–1464, doi:10.1016/j.csr.2007.01.012.
- Palacios, S. L., T. D. Peterson, and R. M. Kudela (2009), Development of synthetic salinity from remote sensing for the Columbia River Plume, *J. Geophys. Res.*, *114*, C00B05, doi:10.1029/2008JC004895.
- Perry, G. D., P. B. Duffy, and N. L. Miller (1996), An extended data set of river discharges for validation of general circulation models, *J. Geophys. Res.*, *101*, 21,339–21,349, doi:10.1029/96JD00932.
- Rawlins, M. A., R. B. Lammers, S. Frolking, B. M. Fekete, and C. J. Vörösmarty (2003), Simulating pan-Arctic runoff with a macro-scale terrestrial water balance model, *Hydrol. Processes*, *17*, 2521–2539, doi:10.1002/hyp.1271.
- Reul, N., S. Saux-Picart, B. Chapron, D. Vandemark, J. Tournadre, and J. Salisbury (2009), Demonstration of ocean surface salinity microwave measurements from space using AMSR-E data over the Amazon Plume, *Geophys. Res. Lett.*, *36*, L13607, doi:10.1029/2009GL038860.
- Reverdin, G., E. Kestenare, C. Frankignoul, and T. Delcroix (2007), Sea surface salinity in the Atlantic Ocean (30°S–50°N), *Prog. Oceanogr.*, *73*, 311–340, doi:10.1016/j.pocan.2006.11.004.
- Richardson, P. L., and G. Reverdin (1987), Seasonal cycle of velocity in the Atlantic North Equatorial Countercurrent as measured by surface drifters current meters and ship drift, *J. Geophys. Res.*, *92*, 3691–3708, doi:10.1029/JC092iC04p03691.
- Richey, J. E., L. A. K. Mertes, T. Dunne, R. L. Victoria, B. R. Forsberg, A. C. N. S. Tancredi, and E. Oliveira (1989), Sources and routing of the Amazon River flood wave, *Global Biogeochem. Cycles*, *3*, 191–204, doi:10.1029/GB003i003p00191.
- Rosario, R. P., M. O. Bezerra, and S. B. Vinton (2009), Dynamics of the saline front in the northern channel of the Amazon River—Influence of fluvial flow and tidal range (Brazil), *J. Coastal Res.*, *SI56*, 1414–1418.
- Salisbury, J. E. (2003), Satellite indices of fluvial influence in coastal waters, Ph.D. thesis, Nat. Resour. and Earth Syst. Sci., Univ. of N. H., Durham, N. H.
- Salisbury, J., D. Vandemark, C. W. Hunt, J. W. Campbell, W. McGillis, and W. McDowell (2008), Seasonal observations of surface waters in two Gulf of Maine estuary-plume systems: Relationships between watershed attributes, optical measurements and surface pCO<sub>2</sub>, *Estuarine Coastal Shelf Sci.*, *77*, 245–252, doi:10.1016/j.ecss.2007.09.033.
- Shipe, R. F., J. Curtaz, A. Subramaniam, E. J. Carpenter, and D. G. Capone (2006), Diatom biomass and productivity in oceanic and plume influenced waters of the western tropical Atlantic Ocean, *Deep Sea Res. Part I*, *53*, 1320–1334, doi:10.1016/j.dsr.2006.05.013.
- Siegel, D. A., S. Maritorena, N. B. Nelson, D. A. Hansell, and M. Lorenzi-Kayser (2002), Global distribution and dynamics of colored dissolved and detrital organic materials, *J. Geophys. Res.*, *107*(C12), 3228, doi:10.1029/2001JC000965.
- Smith, W. O., and D. J. DeMaster (1996), Phytoplankton biomass and productivity and the Amazon River Plume: Correlation with season river discharge, *Cont. Shelf Res.*, *16*, 291–319, doi:10.1016/0278-4343(95)00007-N.
- Subramaniam, A., et al. (2008), Amazon River enhances diazotrophy and carbon sequestration in the tropical North Atlantic Ocean, *Proc. Natl. Acad. Sci. U. S. A.*, *105*, 10,460–10,465, doi:10.1073/pnas.0710279105.
- Twardowski, M. S., and P. L. Donaghay (2001), Separating in situ and terrigenous sources of absorption by dissolved material in coastal waters, *J. Geophys. Res.*, *106*(C2), 2545–2560, doi:10.1029/1999JC000039.
- Vodacek, A., N. V. Blough, M. D. DeGrandpre, E. T. Peltzer, and R. K. Nelson (1997), Seasonal variation of CDOM and DOC in the Middle Atlantic Bight: Terrestrial inputs and photooxidation, *Limnol. Oceanogr.*, *42*, 674–686, doi:10.4319/lo.1997.42.4.0674.
- Vörösmarty, C. J., C. A. Federer, and A. Schloss (1998), Potential evaporation functions compared on US watersheds: Implications for global-scale water balance and terrestrial ecosystem modeling, *J. Hydrol.*, *207*, 147–169, doi:10.1016/S0022-1694(98)00109-7.
- Vörösmarty, C. J., B. M. Fekete, M. Meybeck, and R. B. Lammers (2000), A simulated topological network representing the global system of rivers at 30-minute spatial resolution (STN-30), *Global Biogeochem. Cycles*, *14*, 599–621, doi:10.1029/1999GB900092.
- Wisser, D., B. M. Fekete, C. J. Vörösmarty, and A. H. Schumann (2010), Reconstructing 20th century global hydrography: A contribution to the Global Terrestrial Network-Hydrology (GTN-H), *Hydrol. Earth Syst. Sci.*, *14*, 1–24, doi:10.5194/hess-14-1-2010.
- Yamashita, Y., and E. Tanoue (2004), In situ production of chromophoric dissolved organic matter in coastal environments, *Geophys. Res. Lett.*, *31*, L14302, doi:10.1029/2004GL019734.

J. Campbell, C. Hunt, J. Salisbury, and D. Vandemark, Ocean Processes Analysis Laboratory, University of New Hampshire, 142 Morse Hall, Durham, NH 03824, USA. (joe.salisbury@unh.edu)

B. Chapron and N. Reul, Laboratoire d'Océanographie Spatiale, Institut Français de Recherche et d'Exploitation de la Mer, Centre de Brest, BP 70, Plouzane F-29280, France.

D. Wisser, Water Systems Analysis Group, University of New Hampshire, 8 College Rd., Durham, NH 03824, USA.